High Temperature Performance of Spark Plasma Sintered W0.5(TaTiVCr)0.5 Alloy

Citation: Alvi, Sajid et al. "High Temperature Performance of Spark Plasma Sintered W0.5(TaTiVCr)0.5 Alloy." Metals 10, 11 (November 2020): 1512 © 2020 The Authors

As Published: http://dx.doi.org/10.3390/met10111512

Publisher: MDPI AG

Persistent URL: https://hdl.handle.net/1721.1/128697

Version: Final published version: final published article, as it appeared in a journal, conference proceedings, or other formally published context

metals

MDPI

Article

High Temperature Performance of Spark Plasma Sintered $W_{0.5}(TaTiVCr)_{0.5}$ Alloy

Sajid Alvi [1], Owais Ahmed Waseem [2] and Farid Akhtar [1,*]

[1] Department of Engineering Science and Mathematics, Luleå University of Technology, 97187 Luleå, Sweden; sajid.alvi@ltu.se

[2] Plasma Science and Fusion Center, Massachusetts Institute of Technology, 77 Massachusetts Ave., Cambridge, MA 02139, USA; owaisw@mit.edu

* Correspondence: farid.akhtar@ltu.se

Received: 15 September 2020; Accepted: 8 November 2020; Published: 13 November 2020

Abstract: The phase stability, compressive strength, and tribology of tungsten alloy containing low activation elements, $W_{0.5}(TaTiVCr)_{0.5}$, at elevated temperature up to 1400 °C were investigated. The spark plasma sintered $W_{0.5}(TaTiVCr)_{0.5}$ alloy showed body centered cubic (BCC) structure, which was stable up to 1400 °C using in-situ high temperature XRD analysis and did not show formation of secondary phases. The $W_{0.5}(TaTiVCr)_{0.5}$ alloy showed exceptionally high compressive yield strength of 1136 ± 40 MPa, 830 ± 60 MPa and 425 ± 15 MPa at 1000 °C, 1200 °C and 1400 °C, respectively. The high temperature tribology at 400 °C showed an average coefficient of friction (COF) and low wear rate of 0.55 and 1.37×10^{-5} mm^3/Nm, respectively. The superior compressive strength and wear resistance properties were attributed to the solid solution strengthening of the alloy. The low activation composition, high phase stability, superior high temperature strength, and good wear resistance at 400 °C of $W_{0.5}(TaTiVCr)_{0.5}$ suggest its potential utilization in extreme applications such as plasma facing materials, rocket nozzles and industrial tooling.

Keywords: high-entropy alloy; W-heavy alloy; high-entropy composite; high temperature compression; high temperature tribology; thermal stability

1. Introduction

Tungsten (W) and its alloys possess high melting point, good mechanical properties at elevated temperature, high hardness, low activation in radiation environment and low sputtering yield, which makes it a potential material for various high temperature and nuclear applications [1]. Furthermore, W exhibits low coefficient of thermal expansion, good thermal conductivity and low vapor pressure [2–4]. The advantages of W are coupled with its shortcomings, such as its low fracture toughness, radiation-induced embrittlement, blistering at moderate temperatures by Deuterium (D) and Helium (He), and formation of pits, holes and bubbles by Helium at higher temperatures [5–7]. In order to overcome the shortcomings in W, new strategies on adding different alloying elements to W, such as W-Re [8,9], W-Ta [10,11], W-V [12,13], W-Mo [14,15], W-Cr [16–18] and W-Ti [19,20] binary alloys, W-based composites [21–25], or nanostructure-engineered W [26–28] have been investigated. The reported W-based binary alloys have shown significant improvement in the mechanical properties [19,20]. However, experimental analysis in different aspects of binary alloys have revealed numerous constraints as well, such as irradiation induced embrittlement in W-Re and W-Os, deterioration of mechanical properties due to metastable phases in W-Ti and W-V alloys [1,9]. Similarly, nanocrystalline W has been found to generate He bubble under irradiation leading to poor mechanical properties at high temperatures [27,29]. The laminated, fiber- and net-reinforced W-based

composites have been developed with enhanced toughness and ductility, however, these materials have anisotropic configuration and low relative densities [24,30,31].

The shortcomings of W, W-based alloys and W-composites have made researchers look for alternative promising materials for high temperature applications. Recently, new type of alloys with several principal elements termed as High-Entropy Alloys (HEAs) have been developed [32–34]. The high configurational entropy of mixing in the multicomponent alloy tends to stabilize the formation of simple solid solution of BCC and/or FCC crystal structure [32,35]. HEAs show high yield strength, high hardness, fatigue resistance [36] and good irradiation resistance [37–40]. W-based high-entropy alloys have been developed in the context of high temperature application, showing enhanced high temperature mechanical properties as compared to Ni-based superalloys and nanocrystalline W materials [29,41]. Owais et al., developed a W-based quinary HEA of $W_x(TaTiVCr)_{1-x}$ (x = 0.3 to 0.9) and studied the room temperature mechanical properties [42]. The alloy showed increasing yield strength in the range of 1206–2265 MPa with decreasing W content. Amongst these W-based alloys, $W_{0.5}(TaTiVCr)_{0.5}$ is of particular interest for the fusion applications due to its composition consisting of low activation elements, nearly full relative density, homogeneous microstructure, room temperature compressive strength of ~2100 MPa and hardness of ~788 HV [42,43]. Moreover, its powder metallurgy fabrication does not require high energy milling and make it energy efficient, cost effective and less time consuming [42,43]. The successful application of W in lab-scale fusion devices is proven, therefore, 50 at. % in $W_{0.5}(TaTiVCr)_{0.5}$ makes it more attractive for fusion materials.

High temperature phase stability and mechanical performance is crucial for high temperature applications [3]. For instance, loss of coolant accident (LOCA) in a fusion reactor [44,45] heats materials up to 1200 °C for several days. Therefore, the development of alloys with high temperature phase stability and strength is required for nuclear fusion reactor applications. The sintering mechanism, detailed microstructural and mechanical characterization of $W_x(TaTiVCr)_{1-x}$ (x = 0.3 to 0.9) alloys have been reported in the previous studies [42]. However, the compressive strength and phase stability of $W_{0.5}(TaTiVCr)_{0.5}$ at high temperatures as high as 1400 °C have not been reported so far, which is being presented in this paper. Furthermore, W-alloys are widely used to produce industrial tools such as boring bars and grinding spindles, which require resistance to wear. The published literature on W-based alloys lacks in investigation of room to moderate temperature wear evaluation. And, W-alloys are considered as a potential material for novel mold material for optical glass forming due to its high thermal properties as compared to sintered WC and CVD-SiC used in the market [46]. Thus, we are reporting here the high temperature wear of $W_{0.5}(TaTiVCr)_{0.5}$ alloy at 400 °C, which is in the operational temperature range for molding of optical glass material [47]. The influence of in-situ formed TiC and HEA solid solution on the high temperature wear resistance of $W_{0.5}(TaTiVCr)_{0.5}$ before the onset of oxidation is being presented for the first time. The correlation between 'mechanical and tribological response' and 'microstructural and phase evolution' is discussed.

2. Materials and Methods

2.1. Powders Consolidation

W-based $W_{0.5}(TaTiVCr)_{0.5}$ alloy was developed using elemental powders of W (<1 μm, US Research Nanomaterials, TX, USA), Ta (44 μm, US Research Nanomaterials, TX, USA), V (44 μm, US Research Nanomaterials, TX, USA), Cr (44 μm, US Research Nanomaterials, TX, USA) and Ti (44 μm, Alfa Aesar, USA). The powders were weighed in argon atmosphere and placed in a plastic vials with Si_3N_4 balls in a 1:1 ratio in argon atmosphere, followed by mixing using in-house built planetary ball milling for 1 h. The mixed powders were transferred into a graphite die with 12 mm diameter in argon atmosphere and sintered using SPS (Dr. Sinter SPS 530ET, Fuji Electronic Industrial Co., Ltd., Tsurugashima, Japan). The sintering was carried out at 50 MPa pressure in vacuum of 5.6×10^{-3} mbar at 1600 °C with a heating rate of 100 °C/min and a holding time of 10 min, followed by furnace cooling.

2.2. Structural and Chemical Characterization

X-ray diffraction (XRD) analysis was carried out using Cu-Kα radiation in PANalytical Empyrean operating at 40 kV and 40 mA. Scans were performed between 2θ range of 5 and 100 degrees with 10 mm divergence slit and 1° diffracted beam slits. For high temperature in-situ XRD analysis, HT furnace was installed with W-heating strip. The sample was placed onto a W-heating strip and a heating rate of 10 °C/min was used to increase the temperature up to 1400 °C, where measurements were performed at every 100 °C interval after a holding time of 30 min and measurement time of 40 min. The high temperature in-situ XRD analysis was carried out in vacuum atmosphere (10^{-4} mbar) using Anton Paar HTK 16N strip heater (PANalytical Empyrean, Malvern, UK). The density of the sintered sample was measured using Archimedes' method. In order to carry out selected-area electron diffraction (SAED) pattern analysis, a thin lamella (~50 nm) was prepared by Focused Ion Beam (FIB) milling using Helios Nanolab 600 Dual Beam System (Field Electron and Ion Company, Hillsboro, Oregon, OR, USA), and examined under Transmission Electron Microscope (JEM2100F, JEOL Ltd., Tokyo, Japan). Surface and wear track morphology of the sintered alloy was carried out using scanning electron microscopy (SEM, JSM-IT300LV, JEOL GmbH, Freising, Germany) and energy dispersive X-ray spectroscopy (EDS) with an accelerating voltage of 10–20 kV and working distance of 10 mm.

2.3. High Temperature Mechanical and Tribological Characterization

High temperature compression tests were carried out at 1000 °C, 1200 °C and 1400 °C using Gleeble-3800 (DSI, New York, NY, USA) in vacuum environment with a heating rate and strain rate of 10 °C/s and 10^{-3} s^{-1}, respectively. For high temperature compression tests, cylindrical bars of 4 mm diameter and 6 mm in length were cut using wire electrical discharge machining (EDM) to obtain samples with an aspect ratio of 1.5. Two tests per temperature were performed for repeatability. Tribological tests were performed with a ball-on-disc setup at 400 °C in air atmosphere using universal tribometer (Rtec, San Jose, CA, USA). $W_{0.5}(TaTiVCr)_{0.5}$ sample with 12 mm diameter and 3 mm height was used against a counterball of Al_2O_3 with a diameter of 9.5 mm. The wear tests were carried out at 5 N normal load with a sliding speed of 0.1 m/s for 1 h corresponding to a sliding distance of 600 m. Three tests were performed to examine the repeatability of wear rate and coefficient of friction (COF). The wear depth was calculated using optical profilometry (Wyko NT1100, Bruker Inc., Billerica, MA, US). The wear rate was calculated by the ratio of wear volume to sliding distance and normal load.

3. Results and Discussion

The phase formation and microstructure of $W_{0.5}(TaTiVCr)_{0.5}$ alloy sintered at 1600 °C is shown in Figure 1. The X-ray diffractogram of the sintered alloy showed formation of BCC solid solution with a lattice parameter of 0.314 nm, and formation of TiC phase (Figure 1a). TiC phase forms due to the reaction of liquid Ti with the graphite die during the spark plasma sintering [42]. The relative density of the sintered sample was measured to be 14.1 g/cm^3. The microstructure of the sintered alloy showed formation of three different phases consisting of HEA (grey region), W-rich (bright region) and TiC (black region) phase (Figure 1b). The EDS elemental maps of the alloying elements in the sintered alloy show distribution of elements in W-rich, HEA-phase (marked in red circles in corresponding micrograph), and Ti-rich phase (TiC), in Figure 1c. The formation of HEA-phase (grey region) was further confirmed using EDS point analysis from grey region and bright region, marked as 1 and 2 in Figure 1b respectively, as presented in Table 1.

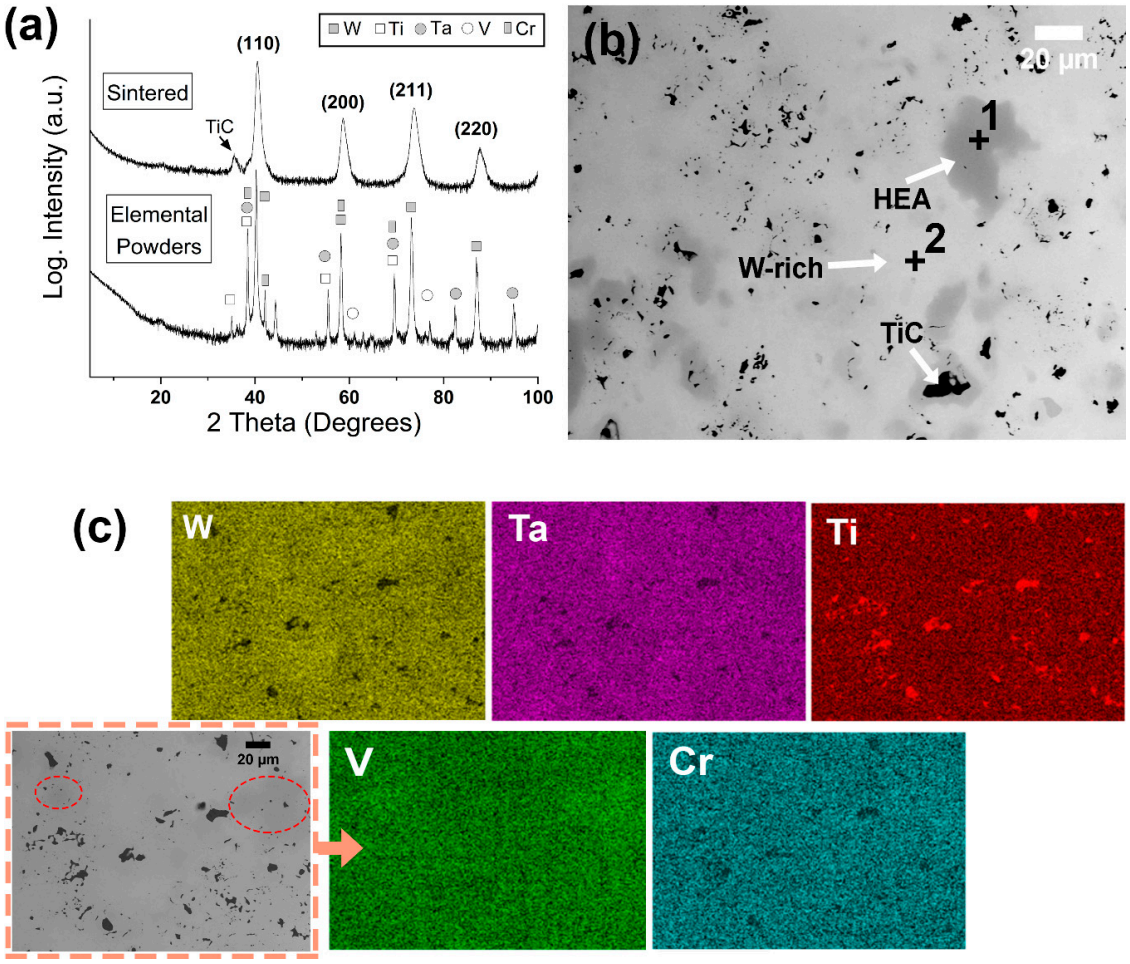

Figure 1. (**a**) X-ray diffraction (XRD) analysis plot, (**b**) backscattered scanning electron microscopy (SEM) micrograph, and (**c**) energy dispersive X-ray spectroscopy (EDS) elemental map of sintered $W_{0.5}(TaTiVCr)_{0.5}$ alloy.

Table 1. EDS analysis of $W_{0.5}(TaTiVCr)_{0.5}$ alloy in Figure 1b in at. %.

Spot	W	Ta	Ti	V	Cr
1	25.7	11.3	9.9	31.8	19.5
2	70.9	5.3	6.8	9.1	7.7

The chemical nature of various regions (W-rich, TiC and HEA) in $W_{0.5}(TaTiVCr)_{0.5}$ alloy was investigated using transmission electron microscopy (TEM). The TEM-EDS and selected-area electron diffraction (SAED) patterns of different regions are shown in Figure 2. The TEM-EDS elemental maps showed uniform distribution of all elements except Ti-rich zone and HEA phase, as shown in Figure 2a. The SAED pattern analysis in W-rich zone from $[011]_{bcc}$ zone axis (ZA) showed BCC reflection with a lattice parameter of 3.14 Å (Figure 2b). The Ti-rich zone with FCC reflection from $[111]_{fcc}$ ZA and a lattice parameter of 4.30 Å (Figure 2c) confirm the formation of TiC phase, identified as black region in Figure 1b,c. The SAED pattern at grey phase, as shown in BSE image of Figure 1b,c, from $[\bar{1}11]$ ZA showed BCC reflection with a lattice parameter of 3.20 Å.

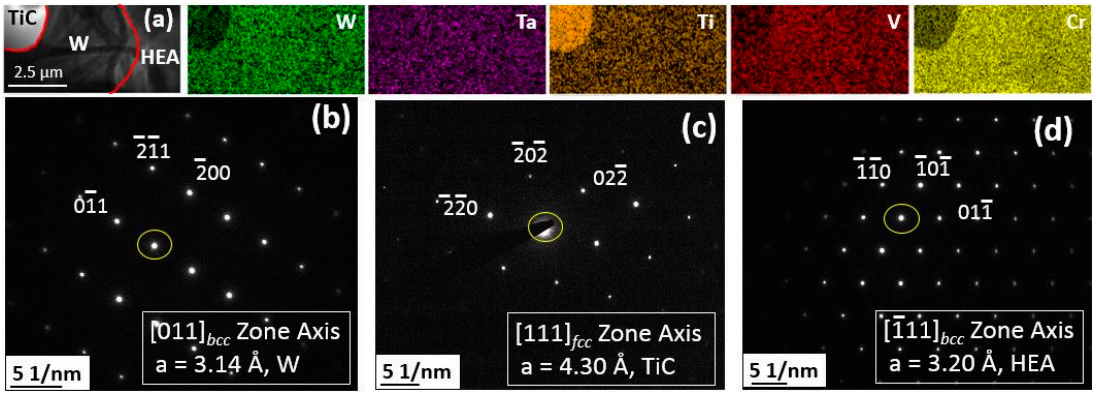

Figure 2. (**a**) Transmission electron microscopy (TEM)-energy dispersive X-ray spectroscopy (EDS) and selected-area electron diffraction (SAED) patterns of (**b**) W-rich, (**c**) TiC, and (**d**) HEA phases observed in $W_{0.5}(TaTiVCr)_{0.5}$.

The in-situ high temperature XRD analysis of $W_{0.5}(TaTiVCr)_{0.5}$ alloy from RT to 1400 °C is shown in Figure 3. The BCC solid solution phase was observed to be stable at all temperatures without the formation of intermetallic phases (Figure 3a). The stability of the alloy up to 1400 °C can be related to high melting point of W, where the composition consists of more than 50 at. % W, which aids thermal stability. Furthermore, the high concentration of other elements enhances the thermal stability through lattice distortion leading to low thermal diffusion in the sintered alloy and enhancing the stability of BCC phase. The formation of TiO_2 was observed after in-situ XRD at 1200 °C, which can be related to softening of Ti leading to its diffusion to the surface and presence of small amount of oxygen in the environment that reacts with Ti on the surface, as shown in Figure 3c and its respective EDS analysis (spot 2) in Table 2 [48]. The SEM-EDS after in-situ high temperature XRD analysis showed the W-rich phase and HEA phase to be stable after the measurement, however the oxide formation in all the phases is observed, as shown in Figure 3c and Table 2. The exact influence of each element at high temperature towards diffusion and oxide formation has yet to be determined and requires further investigation [49].

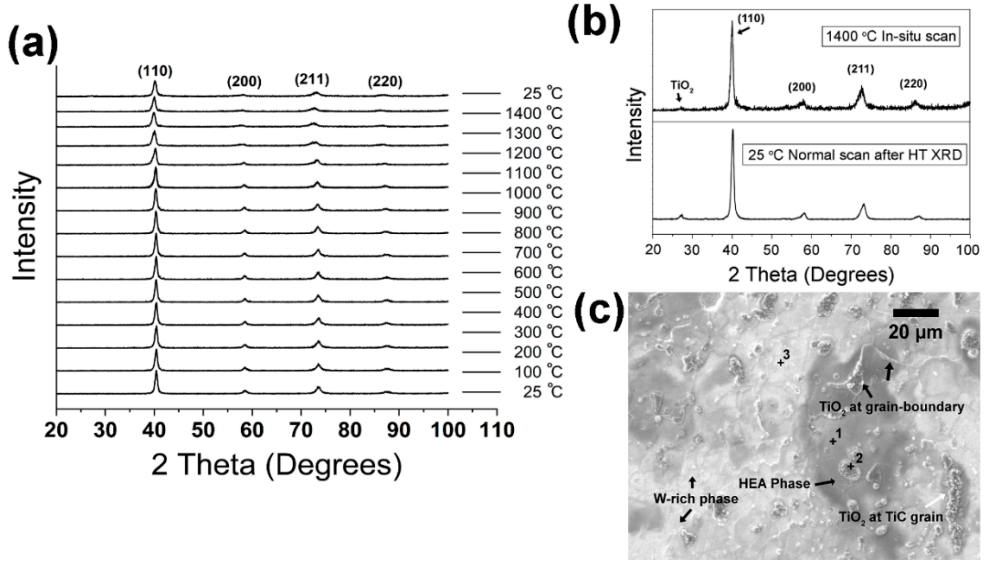

Figure 3. In-situ high temperature XRD analysis from room temperature to 1400 °C showing (**a**) XRD plot at different temperatures, (**b**) XRD pattern collected at 25 °C after in-situ XRD measurements at 1400 °C and in-situ XRD pattern collected at 1400 °C and (**c**) SEM micrograph of surface taken from the specimen after heating to 1400 °C for in-situ XRD measurements.

Table 2. EDS analysis of $W_{0.5}(TaTiVCr)_{0.5}$ alloy in Figure 3 after in-situ XRD measurement at 1400 °C in at. %.

Spot	W	Ta	Ti	V	Cr	O
1	13.1	5.4	7.3	13.1	10.1	5.8
2	0.3	0.1	30.9	2.4	1.0	65.4
3	45.3	4.1	6.3	4.1	6.1	34.0

The engineering stress-strain curves from high temperature compression tests are shown in Figure 4. The sintered alloy showed the highest yield strength of 1136 ± 40 MPa at 1000 °C, followed by yield strength of 830 ± 60 MPa at 1200 °C, and finally yield strength of 425 ± 15 MPa at 1400 °C (Figure 4b). The high temperature compressive strength of $W_{0.5}(TaTiVCr)_{0.5}$ alloy was found to be more than twice that of pure W (~200 MPa at 1350 °C) [50], and higher than previously reported RHEA of NbMoTaW (548 MPa, 506 MPa and 421 MPa at 1000 °C, 1200 °C and 1400 °C, respectively) [51], TaNbHfZrTi (295 MPa and 92 MPa at 1000 °C and 1200 °C, respectively) [52], NbTaTiV (437 MPa at 1000 °C) [53], TaNbVTiAl (~360 MPa and 142 MPa at 1000 °C and 1200 °C, respectively) [54], and VCrFeTaW (182–371 MPa at 1000 °C) [55] due to solid solution strengthening and precipitation strengthening (from in-situ formed TiC phase) [42,56]. The decrease in the yield strength with increasing temperature can be related to the diffusion of Ti, as shown in Figure 3c [49]. The ductility was observed to increase from 6% to 10% with increasing temperature due to thermal softening [57], and Ti diffusion due to its low melting point. Furthermore, the yield strength of $W_{0.5}(TaTiVCr)_{0.5}$ alloy at all temperatures was found to be 3–4 times higher than the previous reported W-based heavy alloys [58,59].

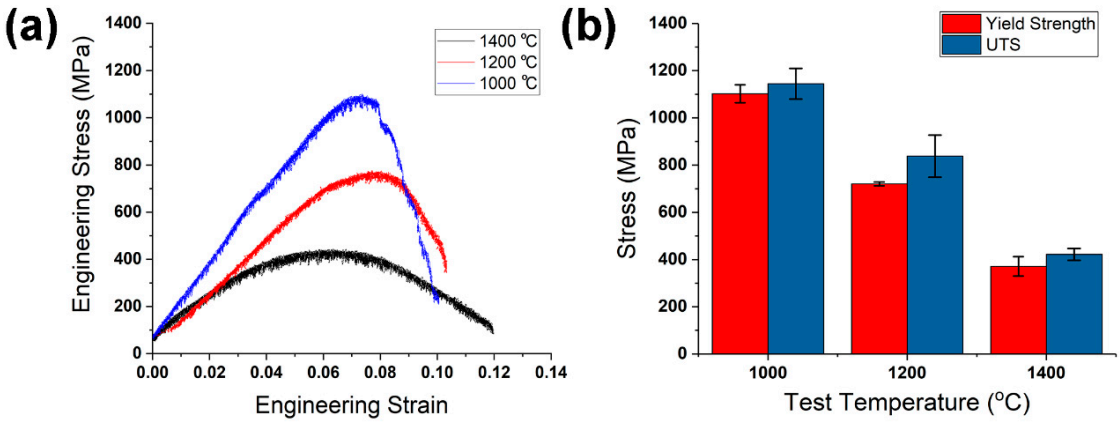

Figure 4. (**a**) High temperature compressive stress-strain plots, and (**b**) yield strength and ultimate tensile strength (UTS) plot of $W_{0.5}(TaTiVCr)_{0.5}$ alloy at different temperatures.

The fracture surface morphologies of specimens after high temperature compression tests are shown in Figure 5 and EDS point analysis from different locations, spot 1–7, marked on fracture surfaces in Figure 5 are presented in Table 3. The fracture surface of the specimen fractured at 1000 °C during compression showed inter-granular fracture around W-rich phase, as shown in Figure 5a,b. The high strength at 1000 °C can be related to the presence of solid solution strengthening and TiC phases (marked as red arrows in Figure 5b and EDS spot 2 in Table 3), which can significantly enhance the impediment of crack propagation [60,61]. A total strain of 0.1 was observed at 1000 °C compression test, higher than total compression strain at RT observed in earlier work [42]. Similar fracture mode was observed at 1200 °C along with a slightly more softening, as shown in Figure 5c,d. However, Ti-rich zone was observed using EDS at grain boundary, as shown in EDS spot 4 in Table 3. A further

increase in the ductility and wetting behavior were observed for the alloy at 1400 °C (Figure 5e,f), which can be due to further softening of HEA-phase, as shown in EDS spot 6 and 7 in Table 3 [62].

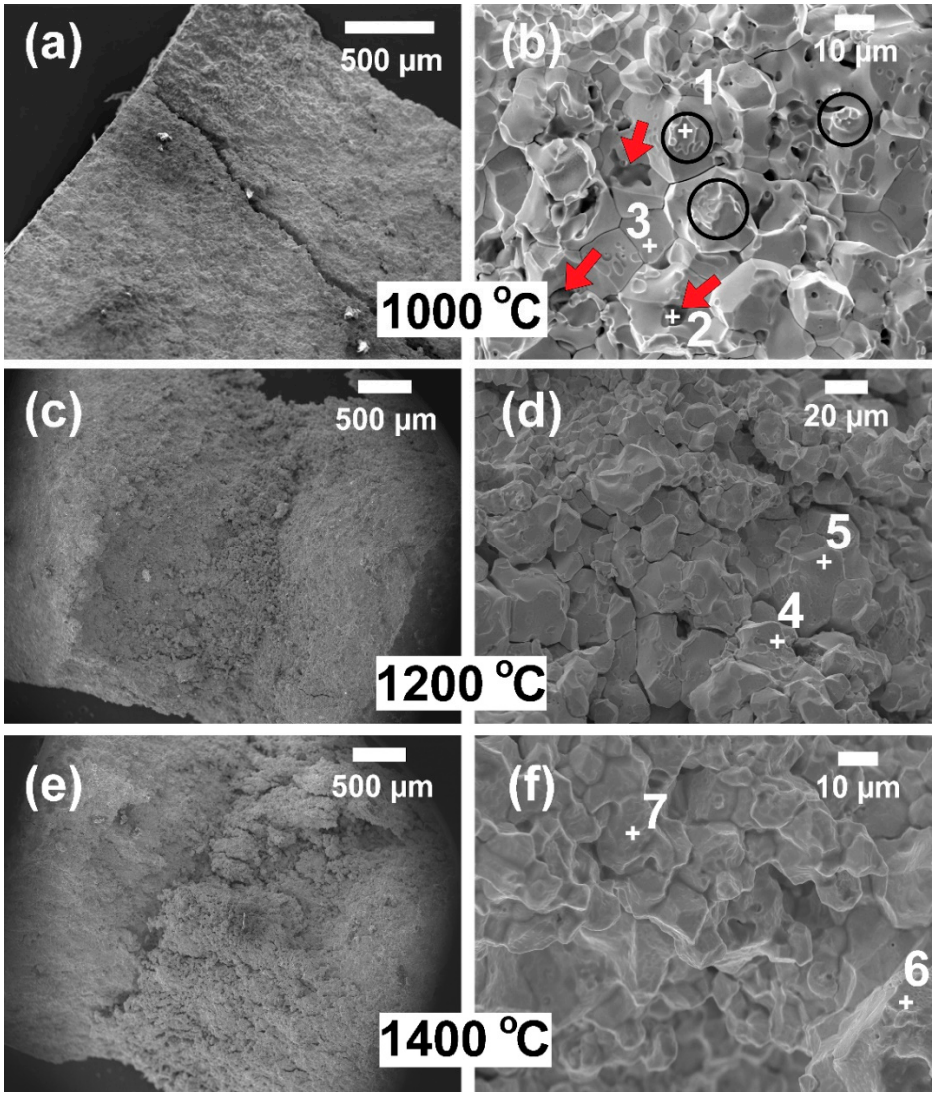

Figure 5. SEM micrographs of fractured surfaces from compression test at (**a**,**b**) 1000 °C, (**c**,**d**) 1200 °C, and (**e**,**f**) 1400 °C.

Table 3. EDS analysis on fracture surface in Figure 5 in at. %.

Spot	W	Ta	Ti	V	Cr
1	41.3	14.8	10.1	19.7	14.2
2	1.9	0.8	94.3	2.3	0.7
3	62.5	14.2	9.2	8.2	5.9
4	14.3	5.1	69.0	6.6	5.0
5	53.1	13.0	10.0	9.6	14.4
6	36.8	15.9	15.4	17.7	14.2
7	44.1	10.3	26.4	12.5	6.7

The high temperature sliding wear test of $W_{0.5}(TaTiVCr)_{0.5}$ alloy at 400 °C against alumina counterball was performed to study the wear behavior before the start of oxidation, as shown in Figure 6. The sliding wear test showed an average COF of 0.55 after an initial run-in period up to 200 m of sliding distance (Figure 6a). The alumina counterball showed a wear scar diameter of 2 mm

arising from high wear induced by $W_{0.5}(TaTiVCr)_{0.5}$ alloy, as shown in Figure 6b. The EDS analysis on alumina counterball showed mostly W transfer layer (spot 1 in Table 4). The wear track morphology of $W_{0.5}(TaTiVCr)_{0.5}$ alloy is shown in Figure 6c,d. The sliding wear showed mild adhesive wear behavior and high amount of alumina counterball transfer, as shown in EDS data of spot 2 and 3 in Table 4. The sliding wear of $W_{0.5}(TaTiVCr)_{0.5}$ alloy against alumina counterball resulted in an average wear rate of 1.37×10^{-5} mm^3/Nm, which was found to be three times lower than the wear rate of pure tungsten (5×10^{-5} mm^3/Nm) at 500 °C as reported by Jiang et al. [63]. Recently, Zhou et al. developed a $(FeCoCrNi)_{1-x}(WC)_x$ (x = 3–11, at. %) composite HEA using SPS to increase the wear properties of FCC based HEA [64]. The study showed enhancement of wear resistance up to 5 at. % WC addition against GCr15 steel counter ball. However, the wear resistance decreased for higher WC content due to lower bonding between reinforcement and HEA matrix phases. In contrast, formation of in-situ TiC reinforcement in HEA matrix has been found to be better for the wear resistance [65–67]. The formation of in-situ carbide reinforcement enhances the mechanical and tribological properties due to stronger bonding between the ceramic reinforcement and metal matrix [68]. Similarly, in this work, formation of in-situ TiC reinforcement, as marked in Figure 6d, coupled with the high hardness (788 HV [36]) from BCC solid solution in $W_{0.5}(TaTiVCr)_{0.5}$ alloy enhanced the wear resistance even at 400 °C.

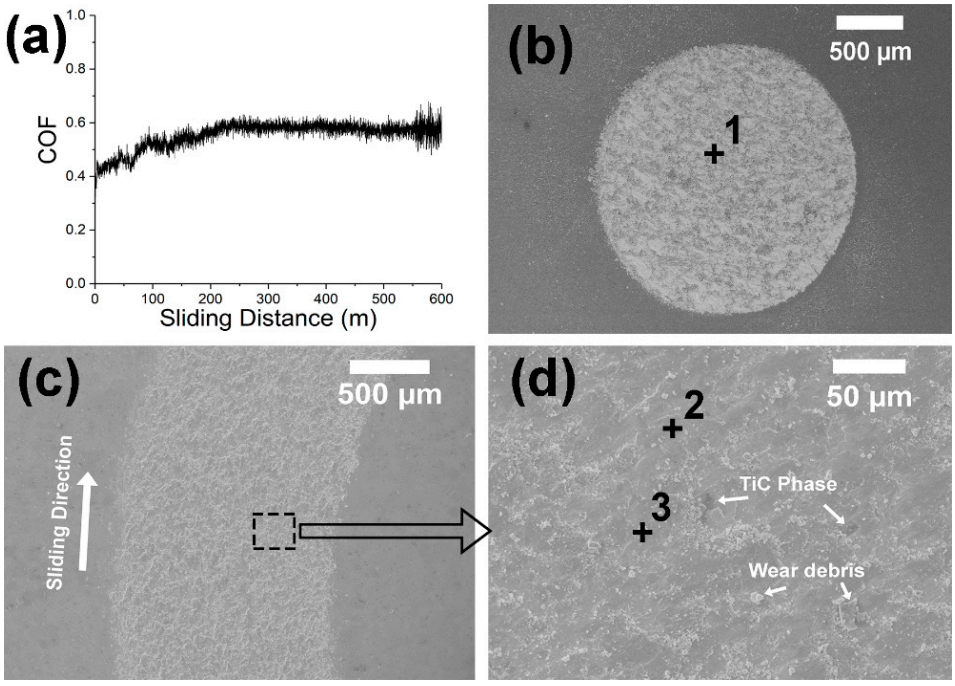

Figure 6. Sliding wear test of $W_{0.5}(TaTiVCr)_{0.5}$ alloy at 400 °C showing (**a**) coefficient of friction (COF) versus sliding distance plot, (**b**) wear scar on alumina counterball, (**c**) wear track morphology and its magnified image in (**d**).

Table 4. EDS analysis on counterball and wear track in Figure 6 in at. %.

Spot	W	Ta	Ti	V	Cr	Al	O
1	9.3	2.8	1.6	1.5	1.9	27.9	54.7
2	9.2	2.8	2.6	2.5	2.5	26.0	54.5
3	17.2	5.5	3.5	3.2	5.6	27.6	37.3

The high temperature studies of $W_{0.5}(TaTiVCr)_{0.5}$ alloy showed high temperature stability of BCC phase up to 1400 °C, high yield strength up to 1400 °C compared to previously reported values, and superior wear resistance at 400 °C. The resulting behavior of $W_{0.5}(TaTiVCr)_{0.5}$ alloy at high temperature shows its promising application in aerospace and fusion plasma facing material. In order

to ensure safety in applications of $W_{0.5}(TaTiVCr)_{0.5}$ alloy, it is required to study its resistance to irradiation, oxidation and erosion as well, which are the topics of our forthcoming studies.

4. Conclusions

In this work, we have studied the elevated temperature performance of spark plasma sintered $W_{0.5}(TaTiVCr)_{0.5}$ alloy. The study of high temperature phase stability using in-situ XRD revealed stable BCC solid solution up to 1400 °C without formation of intermetallic phases. However, formation of TiO_2 was observed after 1200 °C due to higher diffusion rate of Ti compared to other elements at high temperatures. The high temperature compression tests showed high yield strength of 1136 ± 40 MPa at 1000 °C, 830 ± 60 MPa at 1200 °C and 425 ± 15 MPa at 1400 °C due to the presence of in-situ formed TiC phase and solid solution strengthening in W-rich phase and HEA phase. High temperature tribological test at 400 °C showed superior wear resistance due to combination of in-situ TiC phase and HEA solid solution. The wear loss in the alloy was caused mostly by high amount of transfer layer from alumina counterball.

Author Contributions: Conceptualization, S.A., O.A.W. and F.A.; methodology, S.A. and F.A.; software, S.A.; validation, S.A., O.A.W. and F.A.; formal analysis, S.A. and F.A.; investigation, S.A.; resources, F.A.; data curation, S.A.; writing—original draft preparation, S.A.; writing—review and editing, S.A., O.A.W. and F.A.; visualization, S.A.; supervision, F.A.; project administration, F.A.; funding acquisition, F.A. All authors have read and agreed to the published version of the manuscript.

Funding: This work was supported by the Swedish Foundation for Strategic Research (SSF) for Infrastructure Fellowship grant no. RIF14–0083. Farid Akhtar acknowledges The Swedish Foundation for International Cooperation in Research and Higher Education for collaboration with Massachusetts Institute of Technology, USA grant no. IB2019-8546.

Conflicts of Interest: The authors declare no conflict of interest.

References

1. Wurster, S.; Baluc, N.; Battabyal, M.; Crosby, T.; Du, J.; García-Rosales, C.; Hasegawa, A.; Hoffmann, A.; Kimura, A.; Kurishita, H.; et al. Recent progress in R&D on tungsten alloys for divertor structural and plasma facing materials. *J. Nucl. Mater.* **2013**, *442*, 181–189. [CrossRef]
2. Bodryakov, V.Y. Correlation of temperature dependences of thermal expansion and heat capacity of refractory metal up to the melting point: Tungsten. *High Temp.* **2015**, *53*, 643–648. [CrossRef]
3. Antusch, S.; Reiser, J.; Hoffmann, J.; Onea, A. Refractory Materials for Energy Applications. *Energy Technol.* **2017**, *5*, 1064–1070. [CrossRef]
4. Szwarc, R.; Plante, E.R.; Diamond, J.J. Vapor Pressure and Heat of Sublimation of Tungsten. *J. Res. Natl. Bur. Stand. Sect. A Phys. Chem.* **1965**, *69A*, 417–421. [CrossRef]
5. Shu, W.M.; Luo, G.; Yamanishi, T. Mechanisms of retention and blistering in near-surface region of tungsten exposed to high flux deuterium plasmas of tens of eV. *J. Nucl. Mater.* **2007**, *367–370*, 1463–1467. [CrossRef]
6. Nagata, S.; Tsuchiya, B.; Sugawara, T.; Ohtsu, N.; Shikama, T. Helium and hydrogen trapping in W and Mo single-crystals irradiated by He ions. *J. Nucl. Mater.* **2002**, *307–311*, 1513–1516. [CrossRef]
7. Nishijima, D.; Ye, M.Y.; Ohno, N.; Takamura, S. Incident ion energy dependence of bubble formation on tungsten surface with low energy and high flux helium plasma irradiation. *J. Nucl. Mater.* **2003**, *313–316*, 97–101. [CrossRef]
8. Iqbal, Z.; Saheb, N.; Rahman, A. W-25%Re-HfC composite materials for Pin tool material applications: Synthesis and consolidation. *J. Alloys Compd.* **2016**, *674*, 189–199. [CrossRef]
9. Xu, A.; Beck, C.; Armstrong, D.E.J.; Rajan, K.; Smith, G.D.W.; Bagot, P.A.J.; Roberts, S.G. Ion-irradiation-induced clustering in W-Re and W-Re-Os alloys: A comparative study using atom probe tomography and nanoindentation measurements. *Acta Mater.* **2015**, *87*, 121–127. [CrossRef]
10. Dias, M.; Guerreiro, F.; Correia, J.B.; Galatanu, A.; Rosinski, M.; Monge, M.A.; Munoz, A.; Alves, E.; Carvalho, P.A. Consolidation of W-Ta composites: Hot isostatic pressing and spark and pulse plasma sintering. *Fusion Eng. Des.* **2015**, *98–99*, 1950–1955. [CrossRef]
11. Wang, S.; Chen, C.; Jia, Y.L.; Xiao, Z.; Wang, M.P.; Li, Z.; Wu, Y.C. Effects of grain size on the microstructure and texture of cold-rolled Ta-2.5W alloy. *Int. J. Refract. Metals Hard Mater.* **2016**, *58*, 125–136. [CrossRef]

12. Arshad, K.; Zhao, M.; Yuan, Y.; Zhang, Y.; Zhao, Z.; Wang, B.; Zhou, Z.; Lu, G. Effects of vanadium concentration on the densification, microstructures and mechanical properties of tungsten vanadium alloys. *J. Nucle* **2014**, *455*, 96–100. [CrossRef]
13. Arshad, K.; Guo, W.; Wang, J.; Zhao, M.; Yuan, Y.; Zhang, Y.; Wang, B.; Zhou, Z.; Lu, G. Influence of vanadium precursor powder size on microstructures and properties of W–V alloy. *Int. J. Refract. Metals Hard Mater.* **2015**, *50*, 59–64. [CrossRef]
14. Sahoo, P.K.; Srivastava, S.K.; Kamal, S.S.K.; Durai, L. Consolidation behavior of W-20-40 wt.% Mo nanoalloys synthesized by thermal decomposition method. *Int. J. Refract. Metals Hard Mater.* **2015**, *51*, 124–129. [CrossRef]
15. Patra, A.; Meraj, M.; Pal, S.; Yedla, N.; Karak, S.K. Experimental and atomistic simulation based study of W based alloys synthesized by mechanical alloying. *Int. J. Refract. Metals Hard Mater.* **2016**, *58*, 57–67. [CrossRef]
16. Telu, S.; Patra, A.; Sankaranarayana, M.; Mitra, R.; Pabi, S.K. Microstructure and cyclic oxidation behavior of W-Cr alloys prepared by sintering of mechanically alloyed nanocrystalline powders. *Int. J. Refract. Metals Hard Mater.* **2013**, *36*, 191–203. [CrossRef]
17. Zhou, Y.; Sun, Q.X.; Xie, Z.M.; Liu, R.; Wang, X.P.; Fang, Q.F.; Liu, C.S. The microstructure and microhardness of W-5wt % Cr alloy fabricated by spark plasma sintering. *J. Alloys Compd.* **2014**, *585*, 771–775. [CrossRef]
18. Ma, Y.; Han, Q.; Zhou, Z.; Liu, Y. First-principles investigation on mechanical behaviors of W-Cr/Ti binary alloys. *J. Nucl. Mater.* **2016**, *468*, 105–112. [CrossRef]
19. Sahoo, P.K.; Srivastava, S.K.; Kamal, S.S.K.; Durai, L. Microstructure and sintering behavior of nanostructured W-10–20 wt.% Ti alloys synthesized by a soft chemical approach. *Int. J. Refract. Metals Hard Mater.* **2015**, *51*, 282–288. [CrossRef]
20. Dai, W.; Liang, S.; Luo, Y.; Yang, Q. Effect of W powders characteristics on the Ti-rich phase and properties of W-10 wt.% Ti alloy. *Int. J. Refract. Metals Hard Mater.* **2015**, *50*, 240–246. [CrossRef]
21. Song, G.-M.; Zhou, Y.; Wang, Y.-J. Effect of carbide particles on the ablation properties of tungsten composites. *Mater. Charact.* **2003**, *50*, 293–303. [CrossRef]
22. Lee, D.; Park, H.; Ryu, H.; Jeon, S.; Hong, S. Microstructure and mechanical properties of SiC-nanowire-augmented tungsten composites. *J. Alloys Compd.* **2011**, *509*, 9060–9064. [CrossRef]
23. Son, S.J.; Park, K.H.; Katoh, Y.; Kohyama, A. Interfacial reactions and mechanical properties of W–SiC in-situ joints for plasma facing components. *J. Nucl. Mater.* **2004**, *329–333*, 1549–1552. [CrossRef]
24. Reiser, J.; Rieth, M.; Möslang, A.; Greuner, H.; Armstrong, D.E.J.; Denk, T.; Gräning, T.; Hering, W.; Hoffmann, A.; Hoffmann, J.; et al. Tungsten (W) Laminate Pipes for Innovative High Temperature Energy Conversion Systems. *Adv. Eng. Mater.* **2015**, *17*, 491–501. [CrossRef]
25. Basuki, W.W.; Norajitra, P.; Spatafora, L.; Aktaa, J. Fabrication of Tungsten-Vanadium Hybrid Material with Sufficient Toughness for High-Temperature Applications by Diffusion Bonding. *Fusion Sci. Technol.* **2014**, *66*, 315–321. [CrossRef]
26. El-atwani, O.; Gonderman, S.; Suslov, S.; Efe, M.; Temmerman, G.D.; Morgan, T.; Bystrov, K.; Hattar, K.; Allain, J.P. Early stage damage of ultrafine-grained tungsten materials exposed to low energy helium ion irradiation. *Fusion Eng. Des.* **2015**, *93*, 9–14. [CrossRef]
27. El-atwani, O.; Hattar, K.; Hinks, J.A.; Greaves, G.; Harilal, S.S.; Hassanein, A. Helium bubble formation in ultrafine and nanocrystalline tungsten under different extreme conditions. *J. Nucl. Mater.* **2015**, *458*, 216–223. [CrossRef]
28. El-atwani, O.; Suslova, A.; Novakowski, T.J.; Hattar, K.; Efe, M.; Harilal, S.S.; Hassanein, A. In-situ TEM/heavy ion irradiation on ultra fine-and nanocrystalline-grained tungsten: Effect of 3 MeV Si, Cu and W ions. *Mater. Charact.* **2015**, *99*, 68–76. [CrossRef]
29. El-Atwani, O.; Hinks, J.A.; Greaves, G.; Allain, J.P.; Maloy, S.A. Grain size threshold for enhanced irradiation resistance in nanocrystalline and ultrafine tungsten. *Mater. Res. Lett.* **2017**, *5*, 343–349. [CrossRef]
30. Hohe, J.; Gumbsch, P. On the potential of tungsten-vanadium composites for high temperature application with wide-range thermal operation window. *J. Nucl. Mater.* **2010**, *400*, 218–231. [CrossRef]
31. Zhang, L.H.; Jiang, Y.; Fang, Q.F.; Zhang, T.; Wang, X.P.; Liu, C.S. Toughness and microstructure of tungsten fibre net-reinforced tungsten composite produced by spark plasma sintering. *Mater. Sci. Eng. A* **2016**, *659*, 29–36. [CrossRef]

32. Yeh, J.W.; Chen, S.K.; Lin, S.J.; Gan, J.Y.; Chin, T.S.; Shun, T.T.; Tsau, C.H.; Chang, S.Y. Nanostructured high-entropy alloys with multiple principal elements: Novel alloy design concepts and outcomes. *Adv. Eng. Mater.* **2004**, *6*, 299–303. [CrossRef]
33. Cantor, B.; Chang, I.T.H.; Knight, P.; Vincent, A.J.B. Microstructural development in equiatomic multicomponent alloys. *Mater. Sci. Eng. A* **2004**, *375–377*, 213–218. [CrossRef]
34. Ranganathan, S. Alloyed pleasures: Multimetallic cocktails. *Curr. Sci.* **2003**, *85*, 1404–1406.
35. Zhang, B.Y.; Zhou, Y.J.; Lin, J.P.; Chen, G.L.; Liaw, P.K. Solid-Solution Phase Formation Rules for Multi-component Alloys. *Adv. Eng. Mater.* **2008**, *10*, 534–538. [CrossRef]
36. Tsai, M.-H.; Yeh, J.-W. High-Entropy Alloys: A Critical Review. *Mater. Res. Lett.* **2014**, *2*, 107–123. [CrossRef]
37. Jin, K.; Lu, C.; Wang, L.M.; Qu, J.; Weber, W.J.; Zhang, Y.; Bei, H. Effects of compositional complexity on the ion-irradiation induced swelling and hardening in Ni-containing equiatomic alloys. *Scr. Mater.* **2016**, *119*, 65–70. [CrossRef]
38. Kumar, N.A.P.K.; Li, C.; Leonard, K.J.; Bei, H.; Zinkle, S.J. Microstructural stability and mechanical behavior of FeNiMnCr high entropy alloy under ion irradiation. *Acta Mater.* **2016**, *113*, 230–244. [CrossRef]
39. Yang, T.; Xia, S.; Guo, W.; Hu, R.; Poplawsky, J.D.; Sha, G.; Fang, Y.; Yan, Z.; Wang, C.; Li, C.; et al. Effects of temperature on the irradiation responses of Al0.1CoCrFeNi high entropy alloy. *Scr. Mater.* **2018**, *144*, 31–35. [CrossRef]
40. Lu, C.; Niu, L.; Chen, N.; Jin, K.; Yang, T.; Xiu, P.; Zhang, Y.; Gao, F.; Bei, H.; Shi, S.; et al. Enhancing radiation tolerance by controlling defect mobility and migration pathways in multicomponent single-phase alloys. *Nat. Commun.* **2016**, *7*, 1–8. [CrossRef]
41. Senkov, O.N.; Miracle, D.B.; Chaput, K.J.; Couzinie, J.P. Development and exploration of refractory high entropy alloys—A review. *J. Mater. Res.* **2018**, *33*, 3092–3128. [CrossRef]
42. Waseem, O.A.; Ryu, H.J. Powder Metallurgy Processing of a WxTaTiVCr High-Entropy Alloy and Its Derivative Alloys for Fusion Material Applications. *Sci. Rep.* **2017**, *7*, 1926. [CrossRef] [PubMed]
43. Waseem, O.A.; Ryu, H.J. Toughening of a low-activation tungsten alloy using tungsten short fibers and particles reinforcement for fusion plasma-facing applications. *Nucl. Fusion* **2019**, *59*. [CrossRef]
44. Doerner, R.P.; Baldwin, M.; Hanna, J.; Linsmeier, C.; Nishijima, D.; Pugno, R.; Roth, J.; Schmid, K.; Wiltner, A. Interaction of beryllium containing plasma with ITER materials. *Phys. Scr. T* **2007**, *T128*, 115–120. [CrossRef]
45. Baldwin, M.J.; Doerner, R.P.; Nishijima, D.; Buchenauer, D.; Clift, W.M.; Causey, R.A.; Schmid, K. Be-W alloy formation in static and divertor-plasma simulator experiments. *J. Nucl. Mater.* **2007**, *363–365*, 1179–1183. [CrossRef]
46. Suzuki, N.; Haritani, M.; Yang, J.; Hino, R.; Shamoto, E. Elliptical vibration cutting of tungsten alloy molds for optical glass parts. *CIRP Ann. Manuf. Technol.* **2007**, *56*, 127–130. [CrossRef]
47. Budinski, M.K.; Pulver, C.; Nelson, J.J.; Hill, E.G.; Richards, D.A. Glass Mold Material for Precision Glass Molding. Patent US6363747B1, 12 May 2000.
48. Reed, R.C.; Tao, T.; Warnken, N. Alloys-By-Design: Application to nickel-based single crystal superalloys. *Acta Mater.* **2009**, *57*, 5898–5913. [CrossRef]
49. Gawel, R.; Rogal, Ł.; Przybylski, K. Oxidation Resistance of Ti-Al-Cr-Nb-Based High-Entropy Alloys in Air at 1073 K. *J. Mater. Eng. Perform.* **2019**, *28*, 4163–4170. [CrossRef]
50. Wang, J.; Zhao, G.; Chen, L.; Li, J. A comparative study of several constitutive models for powder metallurgy tungsten at elevated temperature. *Mater. Des.* **2016**, *90*, 91–100. [CrossRef]
51. Senkov, O.N.; Wilks, G.B.; Scott, J.M.; Miracle, D.B. Mechanical properties of Nb25Mo25Ta25W25 and V20Nb20Mo20Ta20W20 refractory high entropy alloy. *Intermetallics* **2011**, *19*, 698–706. [CrossRef]
52. Senkov, O.N.; Scott, J.M.; Senkova, S.V.; Meisenkothen, F.; Miracle, D.B.; Woodward, C.F. Microstructure and elevated temperature properties of a refractory TaNbHfZrTi alloy. *J. Mater. Sci.* **2012**, *47*, 4062–4074. [CrossRef]
53. Guo, W.; Liu, B.; Liu, Y.; Li, T.; Fu, A.; Fang, Q.; Nie, Y. Microstructures and mechanical properties of ductile NbTaTiV refractory high entropy alloy prepared by powder metallurgy. *J. Alloys Compd.* **2019**, *776*, 428–436. [CrossRef]
54. Xiang, L.; Guo, W.; Liu, B.; Fu, A.; Li, J.; Fang, Q.; Liu, Y. Microstructure and mechanical properties of TaNbVTiAlx refractory high-entropy alloys. *Entropy* **2020**, *22*, 282. [CrossRef]
55. Zhang, W.; Liaw, P.K.; Zhang, Y. A novel low-activation VCrFeTaxWx (x = 0.1, 0.2, 0.3, 0.4, and 1) high-entropy alloys with excellent heat-softening resistance. *Entropy* **2018**, *20*, 951. [CrossRef]

56. Kang, B.; Kong, T.; Raza, A.; Jin, H.; Hyung, S. Fabrication, microstructure and mechanical property of a novel Nb-rich refractory high-entropy alloy strengthened by in-situ formation of dispersoids. *Int. J. Refract. Metals Hard Mater.* **2019**, *81*, 15–20. [CrossRef]
57. Lennon, A.M.; Ramesh, K.T. The thermoviscoplastic response of polycrystalline tungsten in compression. *Mater. Sci. Eng. A* **2000**, *276*, 9–21. [CrossRef]
58. Li, Y.; Hu, K.; Li, X.; Ai, X.; Qu, S. Fine-grained 93W-5.6Ni-1.4Fe heavy alloys with enhanced performance prepared by spark plasma sintering. *Mater. Sci. Eng. A* **2013**, *573*, 245–252. [CrossRef]
59. Yu, Y.; Ren, C.; Zhang, W. Compressive behavior of liquid phase sintered 90 W-7Ni-3Fe heavy alloy at high temperature and low strain rate condition. *Int. J. Refract. Met. Hard Mater.* **2018**, *76*, 149–157. [CrossRef]
60. Pan, J.; Dai, T.; Lu, T.; Ni, X.; Dai, J.; Li, M. Microstructure and mechanical properties of Nb25Mo25Ta25W25 and Ti8Nb23Mo23Ta23W23 high entropy alloys prepared by mechanical alloying and spark plasma sintering. *Mater. Sci. Eng. A* **2018**, *738*, 362–366. [CrossRef]
61. Yim, D.; Sathiyamoorthi, P.; Hong, S.; Seop, H. Fabrication and mechanical properties of TiC reinforced CoCrFeMnNi high-entropy alloy composite by water atomization and spark plasma sintering. *J. Alloys Compd.* **2019**, *781*, 389–396. [CrossRef]
62. Islam, S.H. Variation of the mechanical properties of tungsten heavy alloys tested at different temperatures. *Rare Met.* **2011**, *30*, 392–395. [CrossRef]
63. Jiang, Y.; Xie, Z.M.; Yang, J.F.; Fang, Q.F. High-temperature tribological behavior of tungsten. *Int. J. Refract. Met. Hard Mater.* **2019**, *84*, 104992. [CrossRef]
64. Zhou, R.; Chen, G.; Liu, B.; Wang, J.; Han, L.; Liu, Y. Microstructures and wear behaviour of (FeCoCrNi)1-x(WC)x high entropy alloy composites. *Int. J. Refract. Met. Hard Mater.* **2018**, *75*, 56–62. [CrossRef]
65. Liu, H.; Liu, J.; Chen, P.; Yang, H. Microstructure and high temperature wear behaviour of in-situ TiC reinforced AlCoCrFeNi-based high-entropy alloy composite coatings fabricated by laser cladding. *Opt. Laser Technol.* **2019**, *118*, 140–150. [CrossRef]
66. Guo, Y.; Li, C.; Zeng, M.; Wang, J.; Deng, P.; Wang, Y. In-situ TiC reinforced CoCrCuFeNiSi0.2 high-entropy alloy coatings designed for enhanced wear performance by laser cladding. *Mater. Chem. Phys.* **2020**, *242*, 122522. [CrossRef]
67. Zhu, T.; Wu, H.; Zhou, R.; Zhang, N.; Yin, Y.; Liang, L.; Liu, Y.; Li, J.; Shan, Q.; Li, Q.; et al. Microstructures and tribological properties of TiC reinforced FeCoNiCuAl high-entropy alloy at normal elevated temperature. *Metals (Basel)* **2020**, *10*, 387. [CrossRef]
68. Fan, Q.C.; Li, B.S.; Zhang, Y. The microstructure and properties of (FeCrNiCo)AlxCuy high-entropy alloys and their TiC-reinforced composites. *Mater. Sci. Eng. A* **2014**, *598*, 244–250. [CrossRef]